


# Oxygen-deficient TiO<sub>2</sub> Yolk-shell Spheres for Enhanced Lithium Storage Properties

Zhaoqian Li, Yuqi Peng, Chaofeng Liu, Xianxi Zhang, Xiuling Li, Yang Huang\* , Yingke Ren\*, Denghui Ji\*, and Guozhong Cao\*

Anatase TiO<sub>2</sub> is a promising anode material for lithium-ion batteries (LIBs) owing to its low cost and stability. However, the intrinsically kinetic limits seriously hindered its lithium-ion storage capability. Here we present that anatase TiO<sub>2</sub> with rich oxygen vacancies can enhance its lithium-ion storage performance. We synthesize anatase TiO<sub>2</sub> with well-retained hierarchical structure by annealing the H<sub>2</sub>Ti<sub>5</sub>O<sub>11</sub>·3H<sub>2</sub>O yolk-shell spheres precursor in nitrogen atmosphere. EPR and XPS data evidence that the oxygen-deficient environment could generate abundant oxygen vacancies in the as-derived anatase TiO<sub>2</sub>, which leads to improved electron conductivity and reduced charge-transfer resistance. The rich oxygen vacancies and high structural integrity of the hierarchical yolk-shell spheres enable the as-derived anatase TiO<sub>2</sub> yolk-shell spheres with a high specific capacity of 280 mAh g<sup>-1</sup> at 100 mA g<sup>-1</sup> and 71% of capacity retention after 5000 cycles at 2 A g<sup>-1</sup>.

## 1. Introduction


Pursuing high power and energy densities for lithium-ion batteries (LIBs) drive academia and industry to develop novel electrode materials for practical applications. Benefiting from its low cost, environmental benignity, wide availability, and chemical stability, TiO<sub>2</sub> attracts broad interests and becomes a promising anode material for LIBs.<sup>[1-6]</sup> However, TiO<sub>2</sub> anode materials still suffer from lower capacity and poor capacity retention over long-term charge-discharge cycles caused by the low ionic and electrical conductivity as well as the intrinsic insertion kinetics limit.<sup>[7,8]</sup> Engineering TiO<sub>2</sub> nanostructures has been demonstrated to be an efficient approach to resolve or alleviate these issues.<sup>[7-10]</sup> Nanoparticles can provide shorter

transport paths for both electronic and Li<sup>+</sup> ions, larger electrode-electrolyte contact area, and in some cases extra interfacial or surface low voltage insertion host for Li<sup>+</sup> ions.<sup>[11-13]</sup> However, severe aggregation of nanoparticles and breaking of particle connections often occurs during the charge-discharge process, leading to new challenges in practical applications.<sup>[10,14]</sup> Recent studies show that hollow structures could mitigate or partly resolve these problems.<sup>[15-23]</sup> Hollow structures including yolk-shell and multi-shell structures composed of nanosized primary building blocks not only hold the advantages of nanoparticles, for example, high surface area and large electrode/electrolyte interface, short electron transfer, and lithium-ion diffusion pathways, but also preserve the integrity of the electrode morphology and possess enhanced volume change accommodation, thus improving lithium-ion storage capability and stability of the electrode materials.<sup>[24-26]</sup>

Another viable strategy to alleviate the low electrical conductivity of anatase TiO<sub>2</sub> is introducing oxygen vacancies. The atomic structure defects resulted from oxygen vacancies can trigger unexpected electronic states changes in TiO<sub>2</sub> electrode materials, thereby providing higher charge mobility. A few studies have been done to explore the effect of oxygen vacancies on the electronic structure and energy storage properties of TiO<sub>2</sub> materials and enhanced electrical conduction on energy storage properties. These results reveal that anatase TiO<sub>2</sub> with rich oxygen vacancies provide greatly improved electrical conductivity and energy storage performance.<sup>[27-29]</sup> Therefore, the combination of primary nanostructures, yolk-shell structure, and abundant oxygen vacancies is a promising approach to improve lithium-ion storage properties of anatase TiO<sub>2</sub>.

In this work, H<sub>2</sub>Ti<sub>5</sub>O<sub>11</sub>·3H<sub>2</sub>O precursor with uniform yolk-shell spherical structure were synthesized by a solvothermal method. The

Dr. Z. Li, Dr. Y. Peng, Prof. Y. Huang  
Key Laboratory of Photovoltaic and Energy Conservation Materials, CAS, Institute of Solid State Physics, Hefei Institutes of Physical Science, Chinese Academy of Sciences, Hefei 230031, China  
E-mail: yhuang@rntek.cas.cn  
Dr. Y. Ren  
College of Science, Hebei University of Science and Technology, Shijiazhuang 050018, China  
E-mail: renyingke@yeah.net  
Dr. X. Zhang  
Shandong Provincial Key Laboratory/Collaborative Innovation Center of Chemical Energy Storage & Novel Cell Technology, School of Chemistry and Chemical Engineering, Liaocheng University, Liaocheng 252000, China  
Dr. C. Liu, Prof. G. Cao  
Department of Materials Science and Engineering, University of Washington, Seattle WA 98195, USA  
E-mail: gzcao@u.washington.edu  
Dr. D. Ji  
College of Physics, Mechanical and Electrical College, Shijiazhuang University, Shijiazhuang City 050035, P. R. China  
E-mail: jidenghui2007@163.com  
Dr. X. Li  
College of Physics and Information Engineering, Hebei Advanced Thin Films Laboratory, Hebei Normal University, Shijiazhuang City 050024, P. R. China  
[Correction added on 4th March 2021, after first online publication: The authors' affiliations have been reordered.]

 The ORCID identification number(s) for the author(s) of this article can be found under <https://doi.org/10.1002/eem2.12156>.

DOI: 10.1002/eem2.12156

precursor can be converted to high crystallinity anatase  $\text{TiO}_2$  with perfectly retained morphology and structure through annealing in a nitrogen atmosphere. The formation of the residual carbon species can efficiently restrict the growth of  $\text{TiO}_2$  crystallites, leading to small primary particles. Synchronously, abundant oxygen vacancies are produced due to the oxygen-deficient environment, which renders improved electrical conductivity and charge transport kinetics. Owing to the abundant oxygen vacancies and high structural integrity yolk-shell spheres structure, the oxygen-deficient  $\text{TiO}_2$  yolk-shell spheres (B-YST) gives rise to enhanced lithium-ion storage performance when compared with the white  $\text{TiO}_2$  yolk-shell spheres (W-YST).

## 2. Results and Discussion

The atomic and electronic properties of pristine  $\text{TiO}_2$  and doped  $\text{TiO}_2$  were first investigated using first-principles calculations. **Figure 1a,b** show the crystal structure of the two models. From the density of states (DOS) in **Figure 1c** and **Figure S1a**, the bandgap of undoped  $\text{TiO}_2$  was calculated to be 3.204 eV, very close to the experimental bandgap value of anatase  $\text{TiO}_2$ , demonstrating the accuracy of our theoretical calculation method. After doping, the  $\text{V}_\text{O}$ -doping decrease the bandgap by 0.493 eV, corresponding to a bandgap of 2.711 eV (**Figure 1d** and **Figure S1b**). The narrowed bandgap will lead to an improved electrical conductivity of the  $\text{V}_\text{O}$  doped  $\text{TiO}_2$ .

**Figure 2a** shows the SEM image of the precursor. The as-obtained sample consists of uniform spheres with an average size of  $\sim 900$  nm. Their yolk-shell characteristic and interior core can be directly observed by SEM in the cracked spheres (**Figure 2b**). Nanosheets are visible and show random orientations in the enlarged

SEM image (**Figure 2c**). The TEM images (**Figure 2d,e**) provide direct evidence for the yolk-shell structures by showing the apparent contrast difference between the hollow shell and the solid core parts. HRTEM observation (**Figure 2f**) near the edge of the yolk-shell sphere reveals that the constituted nanosheets are almost transparent, implying the ultrathin character. The invisible lattice fringe in **Figure S2** demonstrates poor crystallinity of the yolk-shell spheres. XRD pattern (**Figure S3**) can be indexed to the  $\text{H}_2\text{Ti}_5\text{O}_{11}\cdot 3\text{H}_2\text{O}$  (JCPDS NO.44-0130). The broad diffraction peaks with low intensity suggests a poor crystallinity which agrees with the HRTEM observations (**Figure S2**). Thermogravimetric analysis (TG) was conducted to confirm the change of organic residues in the  $\text{H}_2\text{Ti}_5\text{O}_{11}\cdot 3\text{H}_2\text{O}$  yolk-shell spheres with temperature. As shown in **Figure S4**, TG curve can be divided into two stages. The weight loss of ca. 15.2 wt% from room temperature to 250 °C can be assigned to the loss of water,<sup>[30,31]</sup> while the weight loss of ca. 11.2 wt% after 250 °C belongs to the decomposition of organic species, suggesting a ca. 11.2 wt% organic residue existed in the as-obtained sample. The weight loss ending at around 500 °C implies that the residual organic species can be removed at 500 °C.

To elucidate the formation mechanism of such yolk-shell spheres, time-dependent solvothermal experiments were performed. The morphologies and structures of the products obtained at different solvothermal reaction stages were characterized by SEM and TEM. Prior to the heating process, the solution containing IPA, DETA, and TBT maintained a yellow transparent state. At the early solvothermal stage (6 h), as shown in **Figure 3a-d**, the hierarchical spheres formed with a solid core and randomly oriented nanosheets on the surface. After reaction for 12 h, the yolk-shelled spheres with partial interior hollowing appeared (**Figure 3e-h**). A gap distance of  $\sim 100$  nm can be clearly seen by the TEM between the core and the shell (**Figure 3h**). Further extending the reaction time to 24 h gave rise to well-defined yolk-shelled spheres with an enlarged gap distance of ca. 180 nm, accompanied by the shrunken core and increased thickness of the growth of nanosheets on the shell (**Figure 2a-d**). The evolution from the solid to the yolk-shelled spheres stems from an interior etching and outward recrystallization process, namely the inside-out Ostwald-ripening mechanism.<sup>[32,33]</sup> Notably, the existence of diethylenetriamine (DETA) has a great influence on the formation of constituted nanosheets and the uniformity of products. The amino on DETA has a strong coordination effect which can coordinate with titanium source.<sup>[34]</sup> The coordination effect of amino can stabilize the titanium source and inhibit its hydrolysis. Meanwhile, the strong coordination effect of amino on DETA will affect the formation of primary nanostructures and prefer to lead to a nanosheets structure.<sup>[35]</sup> As schematically illustrated in **Figure 3i**, before heating reaction, due to the strong coordination effect of the diethylenetriamine (DETA), the initial solution is transparent, suggesting that no hydrolysis of TBT occurred in this stage. Generally, titanium sources, such as, TBT, TIP can be easily hydrolyzed even trace amounts of water, which will induce irregular morphologies. The

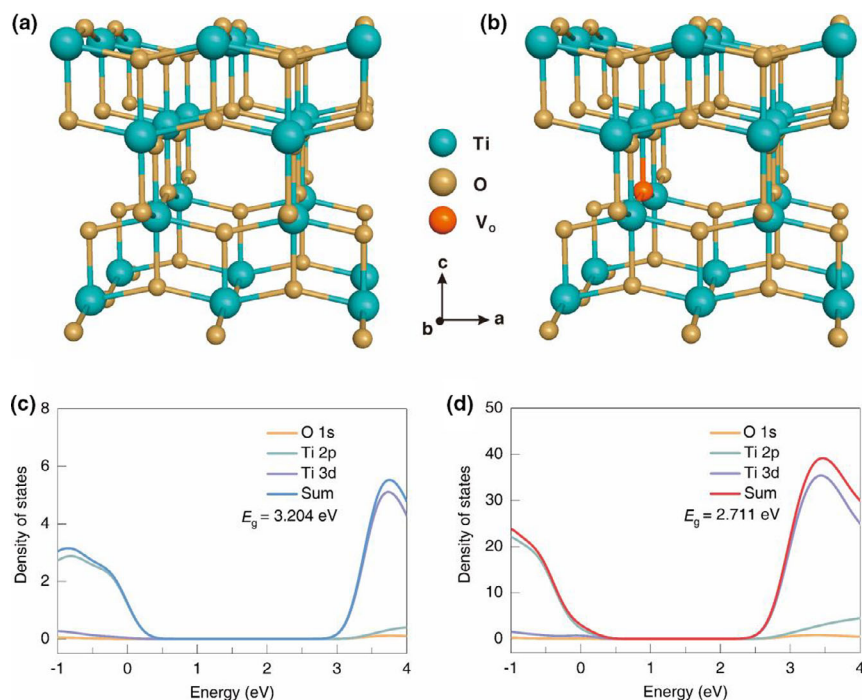


**Figure 1.** Crystal lattice models for a)  $\text{TiO}_2$  and b)  $\text{V}_\text{O}$ - $\text{TiO}_2$  ( $\text{Ti}_{16}\text{O}_{31}$ ). Total density of states (DOS) plots for c)  $\text{TiO}_2$  and d)  $\text{V}_\text{O}$ - $\text{TiO}_2$  obtained by performing PBE + U calculations.

transparent titanium source solution stabilized by DETA can ensure the bottom-up formation of nanostructures during the crystallization process, thus resulted in uniform spheres. Under heating, nucleation and crystallization of Ti composites occur accompanied by the hydrolysis of Ti source due to the etherification of IPA<sup>[36,37]</sup> and the destroyed coordination state of the Ti source, leading to the formation of hierarchical solid spheres. Because the outside nanosheets were protected by the DETA molecules owing to the strong coordination effect, with ongoing the reaction, the interior unstable nanocrystalline will first dissolve and recrystallized on the outward surface, thereby leading the enlarge sphere sizes and increased thickness of the growth of nanosheets on the shell. Meanwhile, the strong coordination effect of DETA molecular with Ti source restricts the primary crystalline growth of the yolk-shelled spheres, resulted in the ultrathin thickness of nanosheets and poor crystallinity as confirmed by XRD analysis (Figure S3).

The pristine  $\text{H}_2\text{Ti}_5\text{O}_{11}\cdot 3\text{H}_2\text{O}$  yolk-shell spheres can be converted to high crystallinity  $\text{TiO}_2$  upon calcination. Previous studies have shown that the selection of annealing atmosphere plays a great role in the morphologies, structure, and properties of the final products.<sup>[38-40]</sup> The formation of residual carbon species by annealing the sample in Ar,  $\text{N}_2$ , or vacuum efficiently affect the growth of  $\text{TiO}_2$  crystallites, leading to different morphologies, structure and the concentration of defects with that annealed in air.<sup>[40,41]</sup> XRD pattern presents sharp characteristic peaks, verifying the improved crystallinity of B-YST and W-YST after calcination (Figure 4a and Figure S5). All the diffraction peaks can be readily indexed well with the anatase  $\text{TiO}_2$  phase (JCPDS No. 21-1272). Compared with W-YST, B-YST shows broader peaks and weaker crystallinity, demonstrating a restrained growth of crystallites. The grain size was calculated to be  $\alpha$ . 10.5 nm according to the Scherrer formula, while the W-YST is  $\alpha$ . 20.3 nm. The existence of residual

carbon in B-YST is confirmed by the TG analysis and the content is examined to be  $\alpha$ . 5.6 wt% (Figure 4b) in a flowing air test. The yolk-shell spherical structure was perfectly retained after annealing (Figure 4c,d). The nanosheets subunits of these yolk-shell spheres can endure the calcination process and still maintain the similar structure with the pristine  $\text{H}_2\text{Ti}_5\text{O}_{11}\cdot 3\text{H}_2\text{O}$  spheres (Figure S6a). Figure 4e,f, and Figure S6b show the hierarchical yolk-shell sphere structure observed by TEM. The smooth and nearly transparent shell edge in Figure S6b demonstrates the ultrathin character of the constituted nanosheets that are almost identical to the pristine  $\text{H}_2\text{Ti}_5\text{O}_{11}\cdot 3\text{H}_2\text{O}$  yolk-shell spheres (Figure 2f). The clear lattice fringes (Figure 4g) demonstrate that B-YST has a high crystallinity after thermal calcination as confirmed by XRD results in Figure 4a. The interplanar distance is measured to be  $\alpha$ . 0.351 nm, corresponding to (101) lattice plane of anatase  $\text{TiO}_2$  (JCPDS No. 21-1272). In contrast to B-YST, although the yolk-shelled spherical morphology is reserved after annealing in air (Figure S7), the constituted nanosheets of the W-YST sample are destroyed and transformed to the coarse particles (Figure S7c,f). As confirmed by the HRTEM (Figure S7g,h), the primary nanoparticles possess a large particle size of  $>20$  nm and high crystallinity with perfect lattice planes.

The presence of oxygen vacancies in the B-YST sample was validated by electron paramagnetic resonance spectroscopy (Figure 4h). Compared with the silent EPR signal in W-YST, the strong EPR signal response with a  $g$  value of 2.002 indicate that rich oxygen vacancies are present in the B-YST sample.<sup>[42-44]</sup> X-ray photoelectron spectroscopy (XPS) analysis of the O1s region evidenced significant differences in the surface of B-YST and W-YST (Figure 4i). As often reported in the case of the oxygen-deficient state, the presence of two O 1s components attributed to Ti-O-Ti in  $\text{TiO}_2$  ( $529.5 \pm 0.2$  eV) and surface OH

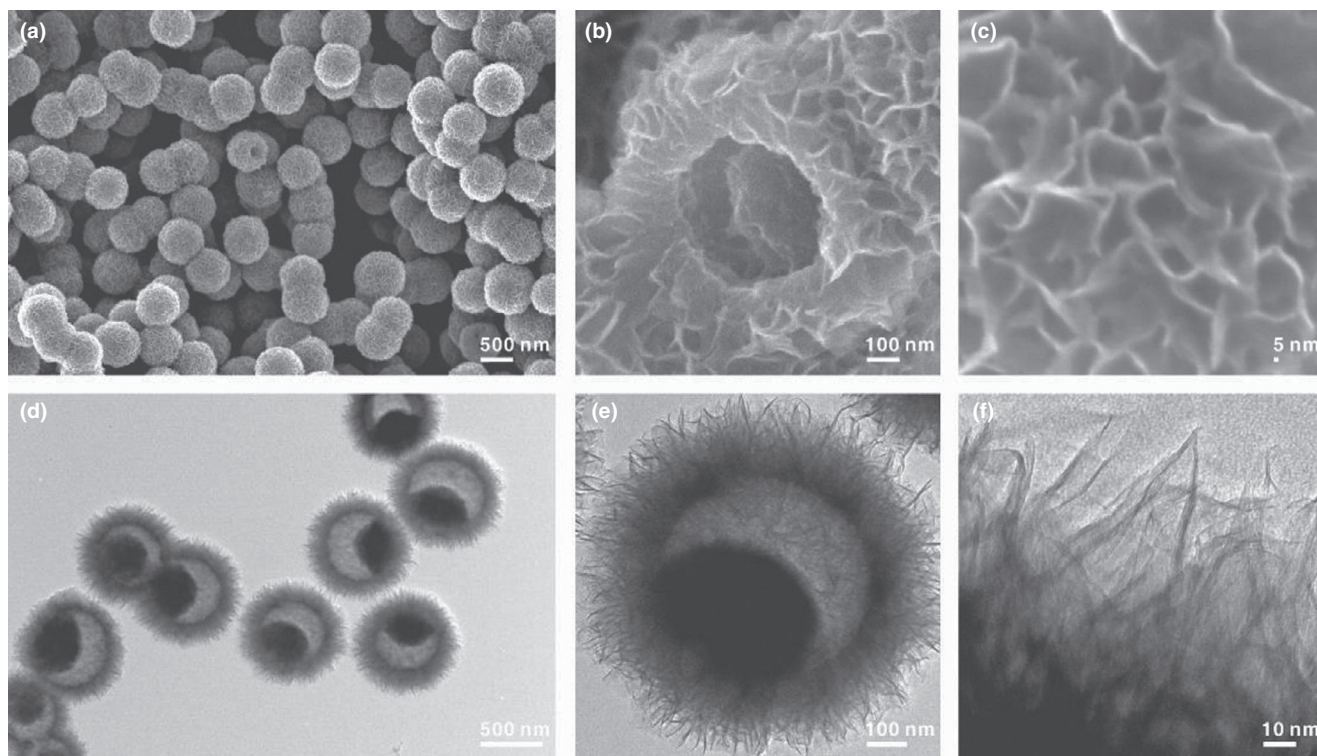


**Figure 2.** a-c) SEM and d-f) TEM images of the  $\text{H}_2\text{Ti}_5\text{O}_{11}\cdot 3\text{H}_2\text{O}$  yolk-shell spheres.

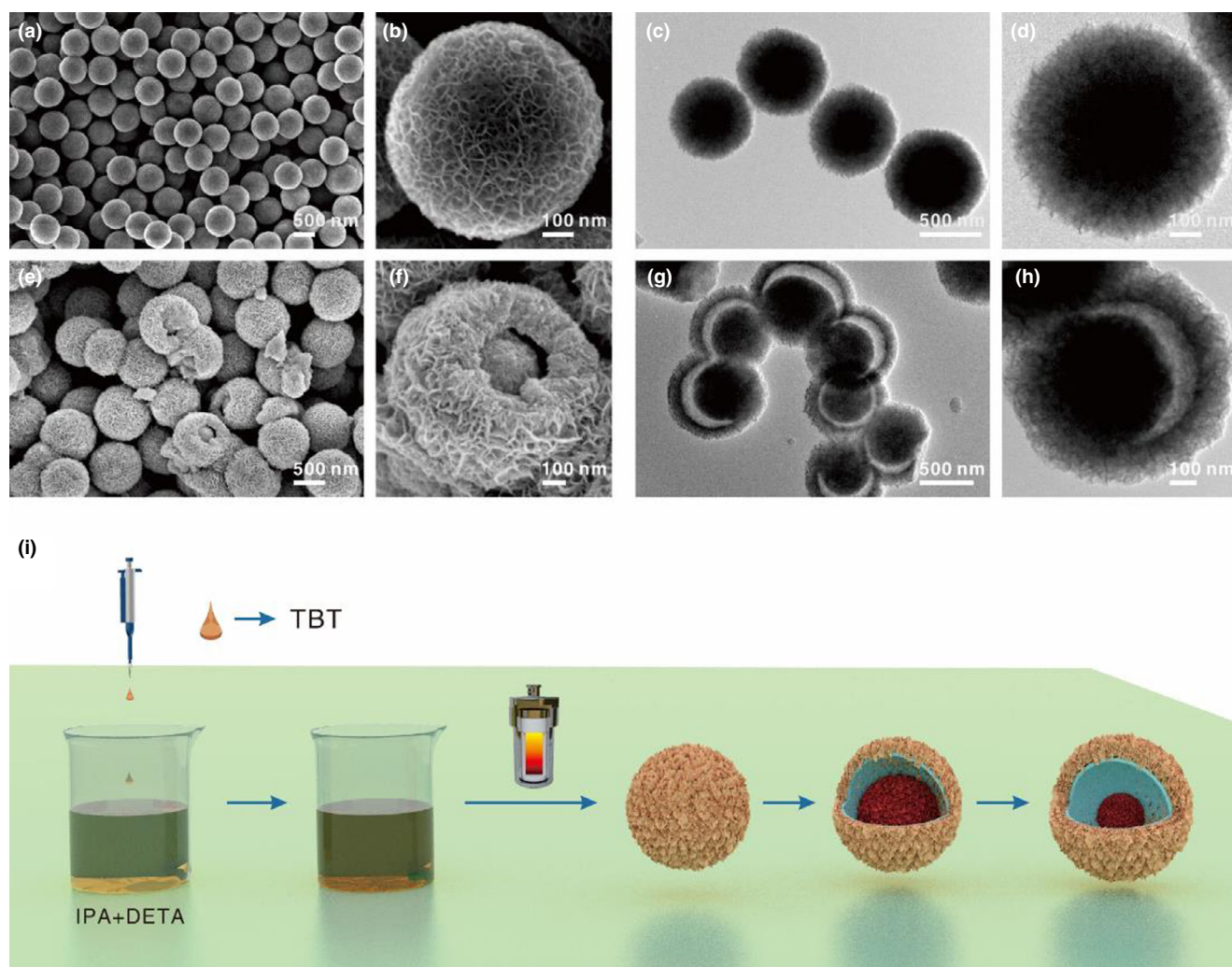


**Figure 3.** SEM and TEM images of the samples prepared at 200 °C for different reaction times: a-d) 6 h, e-h) 12 h. i) Schematic of the formation of yolk-shell spherical precursor. IPA, DETA, and TBT represent isopropyl alcohol, diethylenetriamine, and tetra-*n*-butyl titanate, respectively.

(OOH) species associated with O defects ( $531.0 \pm 0.2$  eV).<sup>[45]</sup> The result revealed by Figure 4i indicates that abundant O vacancies existed in the B-YST sample after heating treatment in N<sub>2</sub>. The proportion of the oxygen vacancies in the B-YST is calculated to be ~33.4% according to the XPS fitting data of O1s, higher than that of W-YST (22.5%). UV-visible absorption spectra (Figure 4j) display that, in comparison with the W-YST sample with an intrinsic absorption edge of  $\alpha$ . 400 nm, the B-YST showed an additional visible light absorptions up to 800 nm, implying a reduced bandgap which agree well with the DFT calculation results. Accordingly, the B-YST and W-YST show black and white color, respectively, as displayed in the inset of Figure 4j. The morphology and structure differences induced by changing the annealing atmosphere are depicted in Figure 4k. The significant difference in two samples demonstrates the great impact of residue carbon species on the structure and properties control of TiO<sub>2</sub> nanomaterials.<sup>[41]</sup>

**Figure 5a** displays discharge-charge voltage profiles at a current density of 100 mA g<sup>-1</sup>. The initial discharge and charge capacities of B-YST are 280 and 224 mAh g<sup>-1</sup>, respectively, corresponding to an

irreversible capacity loss of 20%. The discharge capacity then decays to 254 and 244 mAh g<sup>-1</sup> in the second and third discharge, and remained at 218 mAh g<sup>-1</sup> in the 50th cycle (Figure 5b). This discharge capacity value in the voltage range 1-3 V is higher than previously reported TiO<sub>2</sub> materials, for example, microboxes,<sup>[2]</sup> nanoparticles,<sup>[46]</sup> nanofiber,<sup>[47]</sup> and oxygen-deficient blue TiO<sub>2</sub>.<sup>[48]</sup> However, only an initial capacity of 140 mAh g<sup>-1</sup> (Figure 5a) is obtained by W-YST sample, and then, the capacity decayed to 128 mAh g<sup>-1</sup> in the second discharge and maintained 110 mAh g<sup>-1</sup> in the 50th cycle (Figure 5c). The B-YST exhibits superior rate capability and long-term cyclic performance. When cycled at 0.2-2.0 A g<sup>-1</sup>, capacities of 92-198 mAh g<sup>-1</sup> can be delivered (Figure 5d and Figure S8a). The discharge capacities at each current are higher than those of W-YST (65-108 mAh g<sup>-1</sup>) (Figure 5d and Figure S8b). After cycling at a high rate of 2.0 A g<sup>-1</sup>, a capacity of 196 mAh g<sup>-1</sup> can be recovered upon reducing the current density to 0.2 A g<sup>-1</sup>. Figure 5e shows the cyclic performance of B-YST at 2 A g<sup>-1</sup>, the capacity starts at 90 mAh g<sup>-1</sup> and still maintains at 64 mAh g<sup>-1</sup> after 5000 cycles,

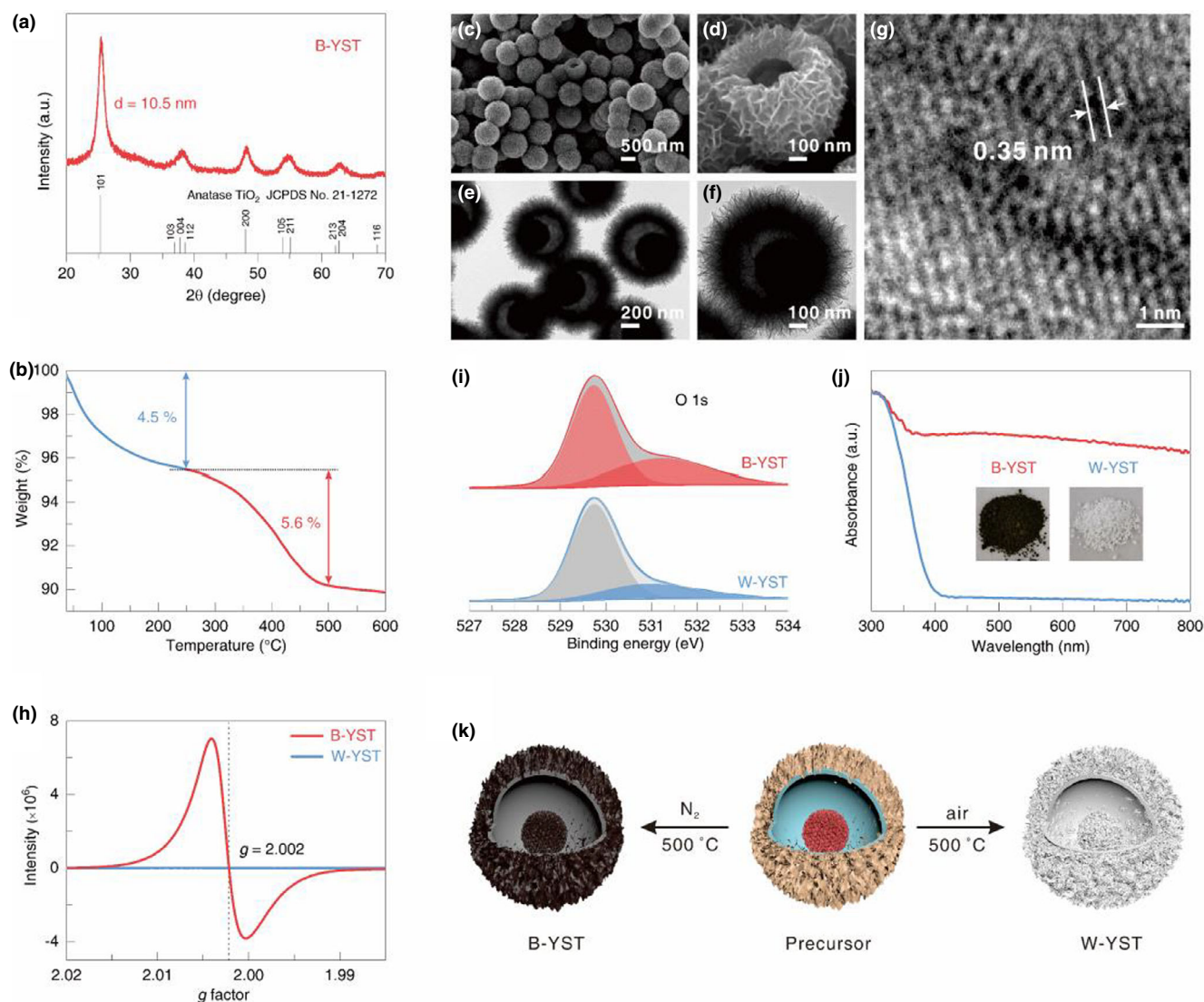


**Figure 4.** a) XRD patterns, b) TG curve, c, d) SEM, e, f) TEM and g) HRTEM images of B-YST. h) EPR, i) O1s XPS and j) UV-Vis absorbance spectra of B-YST and W-YST. The inset of j) is the digital photos of B-YST and W-YST. k) Illustration of the feature changes from the  $\text{H}_2\text{Ti}_5\text{O}_{11}\cdot 3\text{H}_2\text{O}$  precursor to B-YST and W-YST by annealing in  $\text{N}_2$  and air at  $500^\circ\text{C}$ .

corresponding to a capacity retention of 71%. The long-term cycling stability of B-YST demonstrates the robust structural stability of the yolk-shell sphere structure.

The outstanding lithium-ion storage performance of the oxygen-deficient  $\text{TiO}_2$  yolk-shell spheres can be ascribed to the structure and properties control in the calcination process and the advantages of hierarchical yolk-shelled structures. The yolk-shell spheres are composed of primary nanoparticles which can shorten the transport path for the diffusion of  $\text{Li}^+$  ions. The existence of oxygen vacancies in B-YST can provide more accessible active sites for  $\text{Li}^+$  insertion and act as shallow donors, narrowing the bandgap ( $E_g$ ), raising the density of states below the Fermi level, and reducing the charge-transfer resistance, as evidenced by the DFT theoretical calculation, UV-Vis absorption spectra, and EIS measurements (Figure S9). GITT (Figure S10) test confirms that the introduction of oxygen vacancies can enhance  $\text{Li}^+$  diffusion in B-YST, leading to higher  $\text{Li}^+$  diffusion coefficient ranging from  $10^{-8}$  to

$10^{-10} \text{ cm}^2 \text{ s}^{-1}$  than that of W-YST ( $10^{-11}$ – $10^{-8} \text{ cm}^2 \text{ s}^{-1}$ ). The residual carbon in B-YST favor the electrical conductivity of the electrode, leading to improved diffusion coefficient of  $\text{Li}^+$  and fast electron transfer.<sup>[32]</sup> The robust yolk-shell structure effectively inhibits the aggregation of nanoparticles and offers vast space to accommodate the volume change during the charge–discharge process which is responsible for the long-term cycling stability of the electrode and long-term cycling. These features promote the lithium-ion insertion and extraction process and give rise to high-performance lithium-ion storage capability of B-YST.

### 3. Conclusion

A solvothermal approach is presented to synthesized hierarchical  $\text{H}_2\text{Ti}_5\text{O}_{11}\cdot 3\text{H}_2\text{O}$  yolk-shell spheres. Calcined in nitrogen, the precursor

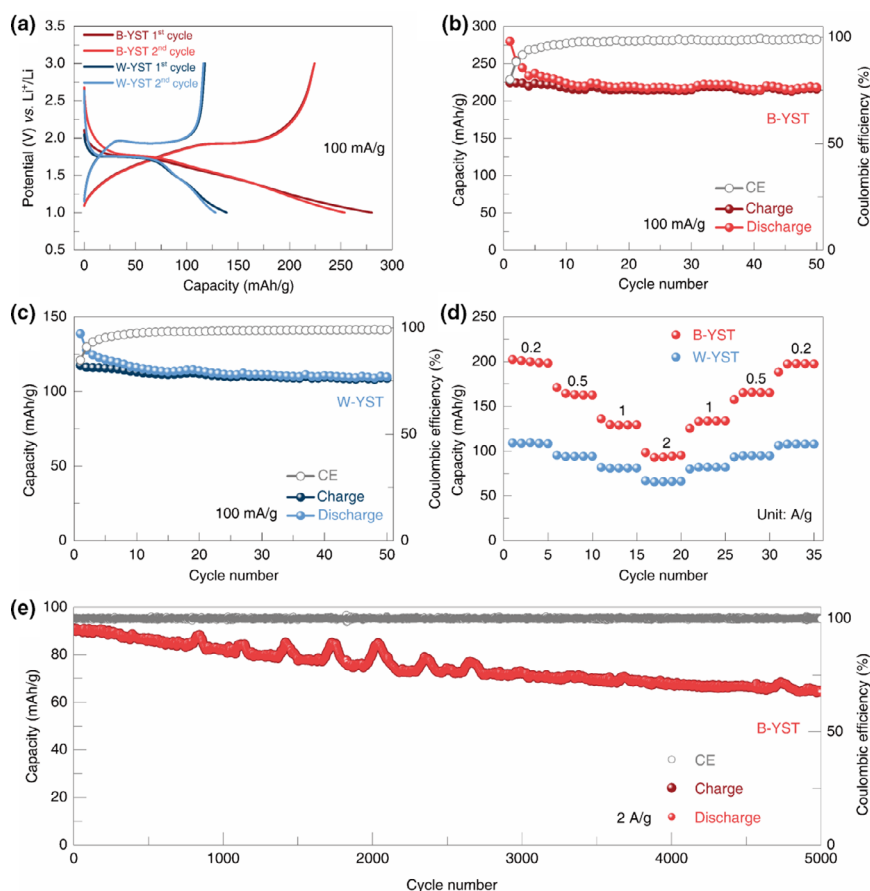


**Figure 5.** a) Charge–discharge curves at  $100 \text{ mA g}^{-1}$  of B-TST and W-YST. b, c) Discharge, charge, and Coulombic efficiency curves of B-YST (b) and W-YST (c) at the current density of  $100 \text{ mA g}^{-1}$ . d) Rate performance of B-YST and W-YST. e) Long-term cycling performance of B-YST at  $2 \text{ A g}^{-1}$ .

can be converted to high crystalline anatase  $\text{TiO}_2$  with well-retained hierarchical yolk-shell sphere structure. The formation of residual carbon species can effectively affect the structure and properties of final  $\text{TiO}_2$  nanomaterials. EPR and XPS data proved that the oxygen-deficient environment leads to the formation of oxygen vacancies in anatase  $\text{TiO}_2$ , which gives rise to improved electron conductivity and reduced charge-transfer resistance. Owing to the rich oxygen vacancies and robust yolk-shell structures, the as-derived  $\text{TiO}_2$  spheres manifest superior lithium storage capabilities with a high and stable capacity of  $280 \text{ mAh g}^{-1}$  at a current rate of  $100 \text{ mA g}^{-1}$  and excellent long-term cyclic stability with a capacity retention of 71% over 5000 cycles at  $2 \text{ A g}^{-1}$ .

## 4. Experimental and Methods

**Calculation Methods:** All calculations were carried out employing the CASTEP plane-wave DFT code.<sup>[49,50]</sup> The generalized gradient approximation functional developed by Perdew and Wang (PW91)<sup>[51]</sup> was chosen as the correlation function, and DFT + U method with a value of Ti was set as 7.0 eV (U) based on the Ref.<sup>[52]</sup> For geometric optimization calculations, a plane-wave basis with a kinetic energy cutoff of was set as 340 eV. The k-points were sampled on Monkhorst–Pack grid of  $2 \times 2 \times 1$  for the unit cell or super cell. The max ionic force, max ionic displacement, and max stress component tolerance were

$8.0 \times 10^{-2} \text{ eV \AA}^{-1}$ ,  $2.0 \times 10^{-3} \text{ \AA}$ , and 0.1 GPa, respectively. It was similar with the method reported by Zhao et al.<sup>[52]</sup>

**Material Preparation: Synthesis of  $\text{H}_2\text{Ti}_5\text{O}_{11} \cdot 3\text{H}_2\text{O}$  Yolk-shell spheres.** In a typical procedure, diethylenetriamine (DETA, Sigma-Aldrich, 0.05 mL) was added dropwise to isopropyl alcohol (IPA, Sigma-Aldrich, 50 mL) with vigorously stirring. After continuous stirring for 10 min, tetra-n-butyl titanate (TBT, Sigma-Aldrich, 2 mL) was added. Continue stirring for 10 min, the resulted transparent yellowish solution was transferred to a 100 mL of autoclave and heated at  $200 \text{ }^\circ\text{C}$  for 24 h in an electric oven. After the reaction, the product was collected and washed with ethanol several times, then dried at  $80 \text{ }^\circ\text{C}$  for 24 h.

**Synthesis of B-YST (Black yolk-shell  $\text{TiO}_2$  spheres):** The as-synthesized yolk-shell spheres were calcined at  $500 \text{ }^\circ\text{C}$  for 1 h in nitrogen with a ramping rate of  $2 \text{ }^\circ\text{C min}^{-1}$ .

**Synthesis of W-YST (White yolk-shell  $\text{TiO}_2$  spheres):** The as-synthesized yolk-shell spheres were calcined at  $500 \text{ }^\circ\text{C}$  for 1 h in air with a ramping rate of  $2 \text{ }^\circ\text{C min}^{-1}$ .

**Material Characterization:** XRD patterns of the products were taken on a Rigaku smartLab X-ray diffractometer 9 kW (Cu K $\alpha$  radiation,  $\lambda = 1.540593$ ). The morphologies and structures were examined by FE-SEM (Helios Nanolab 600i, FEI) and TEM (JEOL, JEM-2100F, 200 kV).  $\text{N}_2$  adsorption–desorption isotherms were measured at 77 K on an ASAP 2460, Micromeritics Instrument. TG analysis was performed using a TA Instruments SDT Q600 from room temperature to  $600 \text{ }^\circ\text{C}$  with a heating rate of  $10 \text{ }^\circ\text{C min}^{-1}$  under a flow of air. XPS analysis was conducted on ESCALAB 250, Thermo-VG Scientific to obtain the chemical states of the oxygen element. The electron paramagnetic resonance (EPR) spectra were taken on a Bruker EMX plus 10/12 (equipped with Oxford ESR910 Liquid Helium cryostat) at 2 K. The UV-Vis absorbance spectra were carried out on a Japan Shimadzu UV-Vis spectrophotometer (UV-2600).

**Electrochemical Measurements:** Electrochemical properties were tested using 2032-type coin cells in the voltage window of 1–3 V. The working electrode was fabricated by mixing and grinding active material (B-YST and W-YST), conductive agent (carbon black, Super-P), and polymer binder (poly(vinylidene difluoride), PVDF, Aldrich) at a weight ratio of 7:2:1. The homogeneous slurry was then coated on a stainless steel mesh and dried at  $80 \text{ }^\circ\text{C}$  for 12 h under vacuum. The mass loading of active materials is  $2\text{--}3 \text{ mg cm}^{-2}$ . The electrode was assembled in an Ar-filled glovebox with the concentrations of moisture and oxygen below 0.5 ppm. Lithium metal was used as the counter electrode. 1 M LiPF $_6$  in a mixture of dimethyl carbonate, ethylene carbonate, and diethyl carbonate (1:1:1 vol%) was used as the electrolyte. Polypropylene film (Celgard 2400) was used as the separator. The galvanostatic discharge/charge was performed on a Neware Battery Testing System (BTS 3000, Shenzhen Neware, China). Cyclic voltammograms (CV) were tested on an electrochemical workstation (CHI600E). EIS spectra were carried out in a frequency range from 100 kHz to 100 mHz with an applied amplitude voltage of 10 mV on a Solartron 1260 Multistat impedance analyzer.

## Acknowledgements

This work was supported by the National Key R&D Program of China (2019YFB1503200), the National Science Foundation (CBET-1803256), the Anhui Provincial Natural Science Foundation (1908085QB52), the CASHIPS Director's Fund (YZJJ2018QN21), Shijiazhuang University Doctoral Scientific Research Start-up Fund Project (20B5019), Colleges and universities in Shandong Province science and technology projects (J17KA097), and CAS Key Laboratory of

Photovoltaic and Energy Conservation, Chinese Academy of Sciences (PECL2018QN006). A portion of this work was performed on the Steady High Magnetic Field Facilities, High Magnetic Field Laboratory, Chinese Academy of Sciences.

## Conflict of Interest

The authors declare no conflict of interest.

## Supporting Information

Supporting Information is available from the Wiley Online Library or from the author.

## Keywords

anatase TiO<sub>2</sub>, lithium-ion batteries, oxygen vacancies, yolk-shell spheres

Received: August 19, 2020  
 Revised: November 2, 2020  
 Published online: November 7, 2020

- [1] J. Mei, T. Liao, L. Z. Kou, Z. Q. Sun, *Adv. Mater.* **2017**, *29*, 1700176.
- [2] X. Gao, G. Li, Y. Xu, Z. Hong, C. Liang, Z. Lin, *Angew. Chem. Int. Ed.* **2015**, *54*, 14331.
- [3] Z. Zhang, P. Xu, H. Zhang, A. Shen, Y. Zhao, *ACS Appl. Energy Mater.* **2019**, *2*, 5744.
- [4] X. Liu, L. Zhao, S. Wang, M. Chao, Y. Li, J. Leng, J. Zhang, Z. Tang, *Sci. Bull.* **2019**, *64*, 1148.
- [5] J. B. Goodenough, H. Gao, *Sci. China Chem.* **2019**, *62*, 1555.
- [6] J. Liu, L. Zhang, H. Li, P. Zhao, P. Ren, W. Shi, P. Cheng, *Sci. China Chem.* **2019**, *62*, 602.
- [7] D.-H. Lee, B.-H. Lee, A. K. Sinha, J.-H. Park, M.-S. Kim, J. Park, H. Shin, K.-S. Lee, Y.-E. Sung, T. Hyeon, *J. Am. Chem. Soc.* **2018**, *140*, 16676.
- [8] J.-Y. Shin, D. Samulielis, J. Maier, *Adv. Funct. Mater.* **2011**, *21*, 3464.
- [9] J. Ye, W. Liu, J. Cai, S. Chen, X. Zhao, H. Zhou, L. Qi, *J. Am. Chem. Soc.* **2011**, *133*, 933.
- [10] G. Zhang, H. B. Wu, T. Song, U. Paik, X. W. Lou, *Angew. Chem. Int. Ed.* **2014**, *53*, 12590.
- [11] Y. S. Hu, L. Kienle, Y. G. Guo, J. Maier, *Adv. Mater.* **2006**, *18*, 1421.
- [12] Y. Ren, Z. Liu, F. Pourpoint, A. R. Armstrong, C. P. Grey, P. G. Bruce, *Angew. Chem. Int. Ed.* **2012**, *51*, 2164.
- [13] H. Ren, R. B. Yu, J. Qi, L. J. Zhang, Q. Jin, D. Wang, *Adv. Mater.* **2019**, *31*, 1805754.
- [14] H. Ren, R. B. Yu, J. Y. Wang, Q. Jin, M. Yang, D. Mao, D. Kisailus, H. J. Zhao, D. Wang, *Nano Lett.* **2014**, *14*, 6679.
- [15] H. Q. Xie, L. F. Hu, F. L. Wu, M. Chen, L. M. Wu, *Adv. Sci.* **2016**, *3*, 1600162.
- [16] Y. L. Xing, S. B. Wang, B. Z. Fang, G. Song, D. P. Wilkinson, S. C. Zhang, *J. Power Sources* **2018**, *385*, 10.
- [17] H. Liu, W. Li, D. K. Shen, D. Y. Zhao, G. X. Wang, *J. Am. Chem. Soc.* **2015**, *137*, 13161.
- [18] X. B. Zhu, J. Y. Tang, H. M. Huang, T. G. Lin, B. Luo, L. Z. Wang, *Sci. Bull.* **2020**, *65*, 496.
- [19] Y. Shan, Y. Li, H. Pang, *Adv. Funct. Mater.* **2020**, *30*, 2001298.
- [20] M. Zheng, H. Tang, L. Li, Q. Hu, L. Zhang, H. Xue, H. Pang, *Adv. Sci.* **2018**, *5*, 1700592.
- [21] X. Xiao, L. Zou, H. Pang, Q. Xu, *Chem. Soc. Rev.* **2020**, *49*, 301.
- [22] T. Zhang, L. Zhang, L. Zhao, X. Huang, Y. Hou, *EnergyChem* **2020**, *2*, 100036.
- [23] J. Hao, X. Li, X. Song, Z. Guo, *EnergyChem* **2019**, *1*, 100004.
- [24] W. W. Gou, X. Z. Kong, Y. P. Wang, Y. L. Ai, S. Q. Liang, A. Q. Pan, G. Z. Cao, *Chem. Eng. J.* **2019**, *374*, 545.
- [25] A. Q. Pan, H. B. Wu, L. Yu, X. W. Lou, *Angew. Chem. Int. Ed.* **2013**, *52*, 2226.
- [26] Y. Cai, H. E. Wang, X. Zhao, F. Huang, C. Wang, Z. Deng, Y. Li, G. Z. Cao, B. L. Su, *ACS Appl. Mater. Interfaces* **2017**, *9*, 10652.
- [27] Y. Wu, Y. Jiang, J. Shi, L. Gu, Y. Yu, *Small* **2017**, *13*, 1700129.
- [28] Q. Chen, B. Ren, Y. Zhao, X. Xu, H. Ge, R. Guan, J. Zhao, *Chem. Eur. J.* **2014**, *20*, 17039.
- [29] Z. Li, Y. Ren, L. Mo, C. Liu, K. Hsu, Y. Ding, X. Zhang, X. Li, L. Hu, D. Ji, G. Cao, *ACS Nano* **2020**, *14*, 5581.
- [30] T. Sasaki, K. M. Yu, Y. Fujiki, *Chem. Mater.* **1992**, *4*, 894.
- [31] H. G. Yang, H. C. Zeng, *J. Am. Chem. Soc.* **2005**, *127*, 270.
- [32] Y. Zhang, C. W. Wang, H. S. Hou, G. Q. Zou, X. B. Ji, *Adv. Energy Mater.* **2017**, *7*, 1600173.
- [33] Z.-Q. Li, W.-C. Chen, F.-L. Guo, L.-E. Mo, L.-H. Hu, S.-Y. Dai, *Sci. Rep.* **2015**, *5*, 14178.
- [34] Y. X. Zhang, X. Guo, X. Zhai, Y. M. Yan, K. N. Sun, *J. Mater. Chem. A* **2015**, *3*, 1761.
- [35] J. S. Chen, Y. L. Tan, C. M. Li, Y. L. Cheah, D. Luan, S. Madhavi, F. Y. C. Boey, L. A. Archer, X. W. Lou, *J. Am. Chem. Soc.* **2010**, *132*, 6124.
- [36] L. E. Mo, Z. Q. Li, Y. C. Ding, C. Gao, L. H. Hu, Y. Huang, T. Hayat, A. Alsaedi, S. Y. Dai, *Sol. Energy* **2019**, *177*, 448.
- [37] H. Li, Z. Bian, J. Zhu, D. Zhang, G. Li, Y. Huo, H. Li, Y. Lu, *J. Am. Chem. Soc.* **2007**, *129*, 8406.
- [38] G. Liu, L. C. Yin, J. Q. Wang, P. Niu, C. Zhen, Y. P. Xie, H. M. Cheng, *Energy Environ. Sci.* **2012**, *5*, 9603.
- [39] Y. Q. Yang, L. C. Yin, Y. Gong, P. Niu, J. Q. Wang, L. Gu, X. Q. Chen, G. Liu, L. Z. Wang, H. M. Cheng, *Adv. Mater.* **2018**, *30*, 1704479.
- [40] B. S. Li, B. J. Xi, Z. Y. Feng, Y. Lin, J. C. Liu, J. K. Feng, Y. T. Qian, S. L. Xiong, *Adv. Mater.* **2018**, *30*, 1705788.
- [41] H. B. Wu, X. W. Lou, H. H. Hng, *Chem. Eur. J.* **2012**, *18*, 2094.
- [42] C. Zhao, Y. Cai, K. Yin, H. Li, D. Shen, N. Qin, Z. Lu, C. Liu, H.-E. Wang, *Chem. Eng. J.* **2018**, *350*, 201.
- [43] J. Chen, Z. Ding, C. Wang, H. Hou, Y. Zhang, C. Wang, G. Zou, X. Ji, *ACS Appl. Mater. Interfaces* **2016**, *8*, 9142.
- [44] Y. Zhang, Z. Ding, C. W. Foster, C. E. Banks, X. Qiu, X. Ji, *Adv. Funct. Mater.* **2017**, *27*, 1700856.
- [45] A. Naldoni, M. Allieta, S. Santangelo, M. Marelli, F. Fabbri, S. Cappelli, C. L. Bianchi, R. Psaro, V. Dal Santo, *J. Am. Chem. Soc.* **2012**, *134*, 7600.
- [46] Y. F. Yuan, F. Chen, S. M. Yin, L. N. Wang, M. Zhu, J. L. Yang, Y. C. Wu, S. Y. Guo, *J. Power Sources* **2019**, *420*, 38.
- [47] Y. H. Wei, H. Chen, H. J. Jiang, B. Y. Wang, H. Liu, Y. Zhang, H. Wu, *ACS Sustain. Chem. Eng.* **2019**, *7*, 7823.
- [48] Z. Hao, Q. Chen, W. Dai, Y. Ren, Y. Zhou, J. Yang, S. Xie, Y. Shen, J. Wu, W. Chen, G. Q. Xu, *Adv. Energy Mater.* **2020**, *10*, 1903107.
- [49] J. P. Perdew, A. Ruzsinszky, G. I. Csonka, O. A. Vydrov, G. E. Scuseria, L. A. Constantin, X. Zhou, K. Burke, *Phys. Rev. Lett.* **2008**, *100*, 136406.
- [50] V. Milman, B. Winkler, J. A. White, C. J. Pickard, M. C. Payne, E. V. Akhramatskaya, R. H. Nobes, *Int. J. Quantum Chem.* **2000**, *77*, 895.
- [51] J. P. Perdew, Y. Wang, *Phys. Rev. B* **1992**, *45*, 13244.
- [52] C. Zhao, D. Huang, J. Chen, Y. Li, Z. Du, *RSC Adv.* **2016**, *6*, 98908.